


# Terahertz multi-beam antenna using photonic crystal waveguide and Luneburg lens

Cite as: APL Photonics **3**, 126105 (2018); <https://doi.org/10.1063/1.5060631>

Submitted: 21 September 2018 . Accepted: 26 November 2018 . Published Online: 17 December 2018

Daniel Headland , Withawat Withayachumnankul , Ryoumei Yamada, Masayuki Fujita, and Tadao Nagatsuma

## COLLECTIONS

 This paper was selected as Featured



View Online



Export Citation



CrossMark

## ARTICLES YOU MAY BE INTERESTED IN

[All-dielectric rod antenna array for terahertz communications](#)

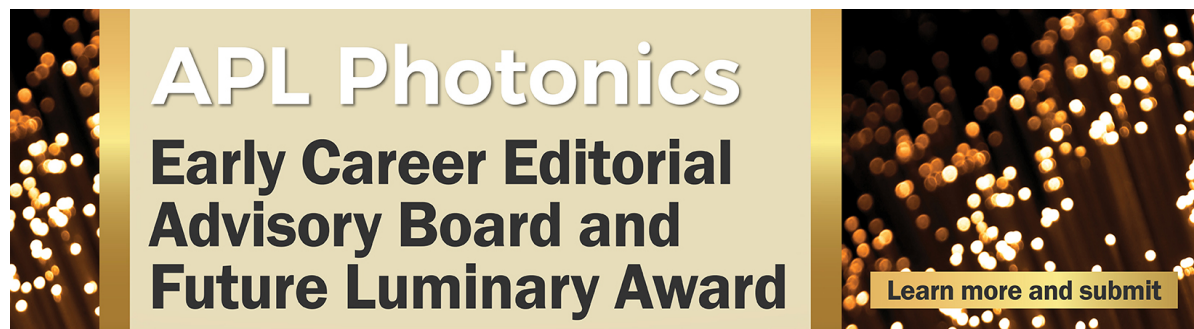
APL Photonics **3**, 051707 (2018); <https://doi.org/10.1063/1.5023787>

[Tutorial: Terahertz beamforming, from concepts to realizations](#)

APL Photonics **3**, 051101 (2018); <https://doi.org/10.1063/1.5011063>

[Broadband and tunable time-resolved THz system using argon-filled hollow-core photonic crystal fiber](#)

APL Photonics **3**, 111301 (2018); <https://doi.org/10.1063/1.5043270>



**APL Photonics**  
**Early Career Editorial  
Advisory Board and  
Future Luminary Award**

[Learn more and submit](#)

# Terahertz multi-beam antenna using photonic crystal waveguide and Luneburg lens

Daniel Headland,<sup>1,2,3,a</sup> Withawat Withayachumnankul,<sup>2</sup> Ryoumei Yamada,<sup>1</sup> Masayuki Fujita,<sup>1,b</sup> and Tadao Nagatsuma<sup>1</sup>

<sup>1</sup>Graduate School of Engineering Science, Osaka University, 1-3 Machikaneyama, Toyonaka, Osaka 560-8531, Japan

<sup>2</sup>School of Electrical and Electronic Engineering, The University of Adelaide, South Australia 5005, Australia

<sup>3</sup>Institute for High-frequency and Communications Technology, University of Wuppertal, North Rhine-Westphalia 42119, Germany

(Received 21 September 2018; accepted 26 November 2018; published online 17 December 2018)

Recent years have seen the emergence of efficient, general-purpose terahertz photonic-crystal waveguides etched from high-resistivity silicon. Systems founded upon this platform will require antennas in order to interface with free-space fields. Multi-beam antennas are desirable to this end, as they are capable of interacting with a number of distinct directions simultaneously. Such functionality can be provided by Luneburg lenses, which we aim to incorporate with the terahertz photonic crystal waveguide. A Luneburg lens requires a precisely defined gradient-index, which we realize using effective medium techniques that are implemented with micro-scale etching of silicon. Thus, the photonic crystal waveguides can be integrated directly with the Luneburg lens and fabricated together from the same silicon wafer. In this way, we develop a planar Luneburg-lens antenna with a diameter of 17 mm and seven evenly spaced ports that cover a 120° field of view. Numerical and experimental characterization confirm that the antenna functions as intended over its operation bandwidth, which spans from 320 to 390 GHz. The Luneburg-lens antenna is subsequently deployed in a demonstration of terahertz communications over a short distance. The device may therefore find applications in terahertz communications, where multiple point-to-point links can be sustained by a given transceiver node. This form of terahertz beam control may also be useful for short-range radar that monitors several directions simultaneously. © 2018 Author(s). All article content, except where otherwise noted, is licensed under a Creative Commons Attribution (CC BY) license (<http://creativecommons.org/licenses/by/4.0/>). <https://doi.org/10.1063/1.5060631>

## I. INTRODUCTION

In recent years, an integrated platform that makes use of high-resistivity silicon photonic crystal slabs has been demonstrated in the terahertz range.<sup>1–5</sup> This platform confines radiation by exploiting a photonic bandgap material, which in this case is implemented using a lattice of through-holes in the silicon slab. Waveguides are formed in this platform by the omission of specific holes, which is a technique that was initially developed in the field of nanophotonics, for operation with optical waves.<sup>6–11</sup> The platform is composed entirely of dielectric materials, and hence the use of a low-loss dielectric such as single-crystal intrinsic silicon<sup>12</sup> yields extremely efficient waveguiding, with propagation loss as low as 0.1 dB/cm in the terahertz range.<sup>3</sup>

The development of this platform is of significant benefit to terahertz technologies. This is because the availability of interconnect—i.e., the capacity to connect two or more devices—is of fundamental importance to the development of a broad range of systems. Many available terahertz

<sup>a</sup>Electronic mail: [headland@ee.es.osaka-u.ac.jp](mailto:headland@ee.es.osaka-u.ac.jp)

<sup>b</sup>Electronic mail: [fujita@ee.es.osaka-u.ac.jp](mailto:fujita@ee.es.osaka-u.ac.jp)

waveguiding structures make use of metals, as is commonplace at lower frequencies. However, this is undesirable for our purposes, as metals are far from ideal conductors at terahertz frequencies, and hence they contribute significant Ohmic loss.<sup>13,14</sup> For example, planar microstrip lines are highly popular in the microwave range, but are typically lossy in the terahertz range.<sup>13,15,16</sup> Hollow-core metallic waveguides are generally more efficient than microstrip lines at terahertz frequencies, and their manufacture is being accelerated by advances in 3D printing.<sup>17</sup> Furthermore, highly specialized 3D-printing techniques can produce hollow-core metallic waveguides with efficiency that is comparable to the aforementioned silicon terahertz photonic crystal waveguides.<sup>18</sup> However, whilst the efficiency of photonic crystal waveguides is relatively stable up to the infrared range,<sup>6,10,19</sup> the loss of hollow metallic waveguides increases markedly as frequency is increased.<sup>20,21</sup> In addition, while hollow metallic waveguides have excellent electromagnetic shielding, they are less readily integrable with other components. For these reasons, we prefer to avoid metals altogether for terahertz waveguiding structures, and instead we focus exclusively on low-loss dielectrics. This approach is likely to ensure scalability across the terahertz range. A variety of all-dielectric waveguides are available in the terahertz range, such as polytetrafluoroethylene (PTFE) hollow-core fibres,<sup>22,23</sup> and they have been found to exhibit extremely high efficiency. However, a rigid, planar platform such as the aforementioned silicon photonic crystal waveguide platform is far more suitable for large-scale manufacture and integration with active terahertz devices. This is critical to realize sophisticated and practical terahertz systems.<sup>5,24</sup>

Previously, this terahertz-range photonic-crystal platform has been employed to accommodate a diverse range of devices, including directional couplers and diplexers,<sup>25</sup> as well as narrowband filters and high-quality-factor sensors.<sup>26–29</sup> Additionally, this platform has been coupled to active devices such as resonant tunneling diodes,<sup>29,30</sup> which are highly compact and have the capacity to operate as both sources and detectors of terahertz radiation.<sup>31–33</sup> Furthermore, advances in coupling structures between resonant tunneling diodes and photonic crystal waveguides have led to coupling efficiency of ~50%, over a bandwidth of several tens of gigahertz.<sup>24</sup> The variety of these early demonstrations is a testament to the general utility and untapped potential of this waveguiding platform. Furthermore, the maximum size available to this platform spans an entire silicon wafer. Thus, it is possible to combine a large number of photonic-crystal-based devices and fabricate them together, to produce a sophisticated, integrated system with numerous interconnecting components.

For a photonic crystal waveguide-based terahertz system to be useful, it must have an interface with free-space fields, i.e., an antenna. Leaky-wave antennas are the most common choice in the nanophotonics regime, where they are known as grating couplers.<sup>34–36</sup> This is because they can be integrated directly into the dielectric waveguide platform, and the fact that they radiate towards broadside provides the device with some aperture. However, all leaky-wave antennas exhibit frequency-scanning, in which the radiation direction is strongly dependent upon frequency, and this is undesirable for applications that demand high bandwidth. Recently, we have demonstrated a terahertz dielectric resonator antenna that was integrated directly into a photonic crystal waveguide.<sup>37</sup> Both the waveguide and the antenna were fabricated from a single silicon slab, resulting in a highly compact and efficient antenna that is free from frequency-scanning. However, the resonant nature of antennas of this sort engenders limitations to both the achievable aperture and operation bandwidth. Following the demonstration of the dielectric resonator antenna, we developed an all-dielectric array of rod antennas, which was similarly integrated directly into the waveguide platform.<sup>38</sup> This antenna exhibited a broad bandwidth, as well as a wide aperture in a single transverse dimension, and hence it addressed the shortcomings of the previous demonstration—albeit at the cost of increased device size.

In general, some form of beam control is beneficial, and indeed necessary, for the overwhelming majority of applications of terahertz waves.<sup>39</sup> For this reason, we aim to incorporate beam control techniques into the photonic crystal waveguide platform in this work. One form of beam control is switched-beam, or multi-beam operation, in which a given antenna can access finitely many distinct far-field directions, often simultaneously. Such functionality is provided by Rotman lens<sup>40,41</sup> and Luneburg-lens antennas,<sup>42–44</sup> which also exhibit a broad bandwidth and wide aperture. This article presents a multi-beam antenna that is implemented using a planar Luneburg lens, which is integrated directly into an all-silicon photonic crystal waveguide.

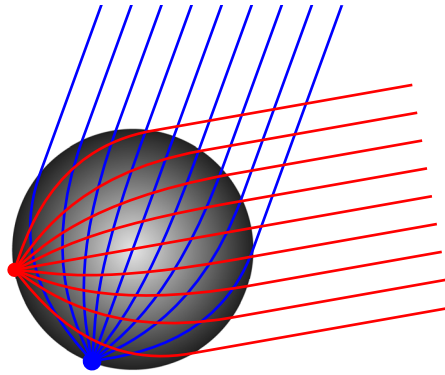


FIG. 1. Luneburg lens concept, showing the reciprocal principle of operation that relates a point on the circumference to a plane wave on the opposite side. It is noted that this behavior is represented with a ray-tracing diagram, but in practice, the lens must be significantly larger than a wavelength for this to be truly valid.

The principle of operation of a Luneburg lens is illustrated in Fig. 1. It is a radially symmetrical device that transforms a point source on its circumference to an outgoing plane wave on the opposite side. Owing to its radial symmetry, a Luneburg lens can perform this beamforming operation in any direction. As it is a passive device, it is also reciprocal, and hence it will also focus an incoming plane wave to a point on the opposite side of its circumference. Another consequence of this passive nature is an innate linearity, and hence it can perform beamforming in various directions simultaneously. A Luneburg lens is a gradient-index (GRIN) device, and hence it is naturally amenable to the all-silicon waveguide platform. This is because the required distribution of refractive index is achievable with effective medium techniques, e.g., with subwavelength through-holes that reduce the effective refractive index.<sup>38,45</sup> It is for this reason that a Luneburg lens is more suitable for integration with the photonic crystal waveguide than the Rotman lens, although the functionality that they provide is broadly equivalent.

Through-hole arrays in high-index dielectrics have previously been deployed as an effective medium for Luneburg-lens antennas in the microwave range.<sup>46</sup> However, a Luneburg lens is generally electrically large, and hence the physical size of a microwave wavelength places such devices at a disadvantage with respect to electronic beamforming techniques. Infrared demonstrations also exist,<sup>47–49</sup> resulting in a far-more compact, nanoscale device. That said, nanoscale structures are not free-standing, and hence these Luneburg lenses required a dielectric substrate for support. This contributed to losses, as well as possible field leakage into the substrate. Furthermore, certain demonstrations<sup>46,49</sup> have made use of transformation optics techniques in order to flatten one side of the Luneburg lens, so as to simplify the interface between the lens and the transceiver chain, and this reduced the field of view to  $60^{\circ}$ – $70^{\circ}$ . In this work, we maintain the radial symmetry of the Luneburg lens, yielding a  $120^{\circ}$  field of view. The Luneburg lens is integrated directly with seven photonic crystal waveguides, resulting in an efficient multi-beam antenna with an operation bandwidth from 320 GHz to 390 GHz. Aside from field confinement, the use of photonic crystals provides benefits to mechanical stability, which renders the device entirely free-standing and self-supporting. This, combined with the fact that a terahertz wavelength is smaller than a millimeter, results in a highly manageable and practical antenna.

## II. ANTENNA DESIGN

### A. Lens body

The Luneburg-lens portion of the antenna is henceforth referred to as the “lens body” in the context of the terahertz Luneburg-lens antenna that is the subject of this article. In order to design this component of the antenna, we have made use of an all-analytical methodology that does not require any form of numerical optimization.

There are two main constituents to the design of the lens body; one must first obtain the required distribution of refractive index inside the lens body, and then one must determine a practical means to achieve this bespoke index distribution. Analytical solutions exist for the first concern and are given in the Appendix. In general, the refractive index distribution in a Luneburg lens is at maximum in the center of the lens, and it progressively heads to its minimum value towards the outer edge. Although the initial solution derived by R. K. Luneburg dictates that the index must head to unity at the lens circumference,<sup>42</sup> this is challenging to achieve with GRIN media in practice. Fortunately, more-general solutions exist that allow one to prescribe a specific value of refractive index at this edge point and then derive the required refractive index for all other points inside the lens.<sup>46,50</sup> Several such solutions, for different values of edge-index, are given in Fig. 2(a). It is noted that the solutions conveniently scale with respect to any choice of maximum lens-body radius. The lens radius is selected to be 8.5 mm for this design, which is  $\sim 10\lambda$  in the frequency range of interest. Thus, the antenna is of reasonable electrical size for the purposes of antenna gain, whilst remaining small enough to simulate numerically for verification purposes.

In order to realize the required refractive index distribution, we make use of an array of densely packed, subwavelength through-holes in a silicon slab. These holes are cylindrical and are arranged into a periodic triangular lattice for mechanical integrity. This structure is chosen because a host medium that is infiltrated with subwavelength inclusions of a different medium will be experienced by an electromagnetic wave as an effective medium. The electromagnetic properties of this effective medium will lie in-between those of the constituent media and are dependent upon the volumetric fill factor of the inclusions.<sup>51–55</sup> In this case, these media are silicon and air, and the fill factor is dictated by hole diameter and spacing. Effective medium theory yields an effective bulk refractive index, which describes the propagation of a TEM wave. However, the radiation does not propagate as a TEM wave inside the lens body due to the finite thickness of the silicon slab, which in this case is equal to  $200\ \mu\text{m}$ . Rather, the waves are confined into a moderately dispersive  $\text{TE}_0$  slab mode, which is so-designated because the electric field vector is parallel to the slab's top and bottom surfaces. As such, this effective bulk refractive index must be converted to an effective modal index. The mathematical procedure

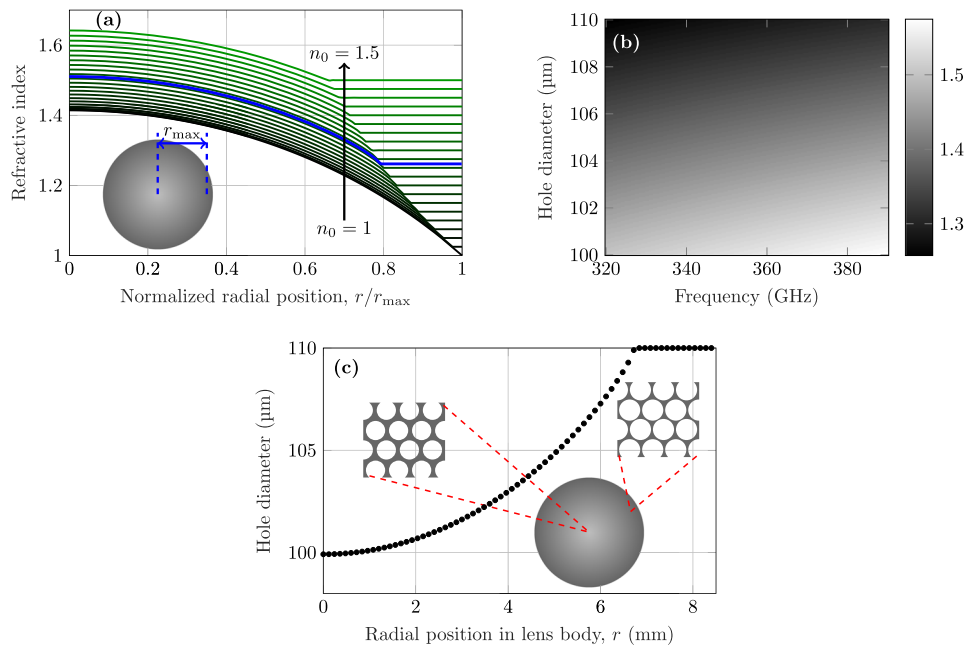


FIG. 2. Design of Luneburg lens body. (a) Required index as a function of radial position, for a range of edge-index values  $n_0 = n(r_{\text{max}})$  that are stepped in intervals of  $\Delta n = 0.025$ , (b) the relationship between the hole diameter and the effective modal index of the  $\text{TE}_0$  slab waveguide mode in the  $200\ \mu\text{m}$ -thick effective medium, which is a triangular hole lattice with period  $120\ \mu\text{m}$ , and (c) hole diameter,  $D_{\text{hole}}$ , as a function of lens radius  $r$ , at sampling intervals of the lattice period  $120\ \mu\text{m}$ , for chosen design parameters of  $r_{\text{max}} = 8.5\ \text{mm}$  and  $D_{\text{hole,max}} = 110\ \mu\text{m}$ . This design corresponds to the blue curve in (a).

that is employed to calculate the effective bulk- and modal-indices is given in the [Appendix](#). For this particular design, we make use of  $120\ \mu\text{m}$  hole separation, which is equal to a half-wavelength in bulk silicon at  $\sim 365\ \text{GHz}$  and is subwavelength over the operation bandwidth. The resulting effective modal index as a function of hole diameter and frequency is given in Fig. 2(b). It is noted that, whilst there is some variation in the effective modal index with respect to the frequency (i.e., dispersion), this is far less pronounced than the variation that is dependent upon the hole diameter. Thus, this medium can be considered mildly dispersive, as is common for slab-mode waveguides.<sup>56</sup>

It is desirable for the Luneburg lens to have an edge index that is as low as possible, so as to minimize reflections at the interface to free space. Thus, the proportion of silicon at the edge is minimized by selecting a suitably large hole diameter. However, the index cannot be reduced to unity, as we must maintain enough silicon such that the antenna remains mechanically stable. With these constraints in mind, the maximum hole diameter is set to  $110\ \mu\text{m}$ , which yields an edge index that ranges from  $n_0 = 1.2$  to  $1.35$  across the operation bandwidth. For these values of refractive index, we expect that less than 2.2% power, or  $-16.6\ \text{dB}$ , is reflected at the circumference of the lens.

Finally, this calculation of effective modal index is employed to map the required index distribution for a Luneburg lens in Fig. 2(a) to the corresponding hole diameter, as a function of radial position in the lens body. This procedure must be carried out at a specific design frequency, as the modal index is mildly dispersive. As such, detuning away from this design frequency will cause the refractive index to deviate gradually from the desired distribution. However, as this variation is minor, the distribution of refractive index is expected to maintain approximate adherence to the desired case of the Luneburg lens design. In this instance, the design frequency is chosen to be  $325\ \text{GHz}$ . It is noted that this is close to the lower-end of the operation bandwidth for this device, where the propagation loss in the photonic crystal waveguide is minimal due to the absence of leaky modes.<sup>3</sup> As a result of this, the peak deviation from the desired refractive index due to dispersion is 4.3%, whereas a design frequency in the center of the operation bandwidth would reduce this deviation to 2.5%. The resulting distribution of hole diameters for this Luneburg lens design procedure is plotted in Fig. 2(c). It is noted that the range of hole diameters is not especially large, as it spans from  $100$  to  $110\ \mu\text{m}$ .

## B. Feed

The Luneburg lens is fed via terahertz photonic-crystal waveguides, for which the design details have been given in numerous previous publications.<sup>3,25,29</sup> In brief, a  $200\ \mu\text{m}$ -thick high-resistivity silicon wafer is perforated with a periodic, triangular lattice of cylindrical through-holes, as with the previously discussed effective medium. The sole distinction between these two media lies in their geometric parameters; the photonic crystal's through-holes are  $144\ \mu\text{m}$  in diameter and are spaced  $240\ \mu\text{m}$  apart. This forms a photonic bandgap material, i.e., a medium in which, over a specific bandwidth, no propagating electromagnetic mode can exist. This medium can therefore be considered as a dielectric mirror for in-plane terahertz waves. It is noted that, whilst the pitch of the photonic crystal is twice that of the aforementioned effective medium, the holes themselves are of similar size. This is an interesting fact, as it shows clearly how critical the pitch of the hole array is to device operation—larger pitch produces a dielectric mirror and smaller pitch produces a GRIN medium.

Having formed the photonic bandgap material, a single row of cylindrical holes is subsequently omitted to produce a narrow track along which propagating modes are supported. Thus, the defect row left by the absent holes is essentially a dielectric waveguide. The resulting waveguide is highly efficient, having been shown to exhibit loss as low as  $0.1\ \text{dB/cm}$ , and has the capacity to support turns and corners with low reflection and radiation losses.

A tapered feed structure interfaces the lens body with the photonic crystal waveguide. In contrast to the wholly analytical design methodology that the lens body enjoys, this feed is designed empirically using numerical simulations. A diagram of the feed structure is given in Fig. 3. There are two main considerations for the feed design. First, we wish to match the modal index of the waveguide to the lens body in order to minimize reflections. Second, it is desirable to have a field distribution at the feed point that approximates a point source, so as to properly utilize the beamforming functionality offered by the Luneburg lens. Both of these considerations must hold in broadband.

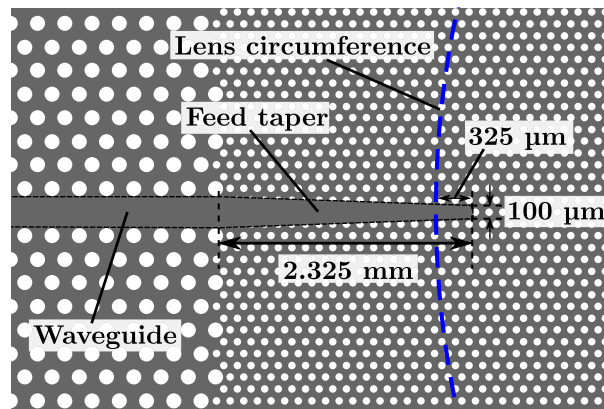


FIG. 3. Design of the tapered feed structure, showing the photonic crystal waveguide and the lens circumference. The effective medium at the outer edge of this circumference is extended to meet the photonic crystal slab, for mechanical stability.

To address the matching requirement, we note that the phase velocity in the photonic crystal waveguide is lower than that in the lens body. If the two media were introduced directly, then this would cause reflections, as a backward-travelling component is generated when the boundary conditions are enforced. Thus, in order to match between these media in broadband, the feed must transition smoothly between their phase velocities. To this end, the width of the waveguide track is tapered prior to its point of contact with the lens body, as this technique gradually accelerates the phase velocity of the guided wave such that, at the termination of the feed structure, the phase velocity is matched to that of propagating waves at the edge of the lens body. If the waveguide were to taper all the way to a sharp tip, then it would be matched to free-space. Thus, due to the greater-than-unity effective modal index in the lens body, the terminating width of the taper is finite, and hence it exhibits a snub-nosed appearance. Note that it is not possible to taper the photonic crystal waveguide track directly whilst maintaining the surrounding photonic crystal structure, as the width of this track is set by the omission of a single row of holes in the photonic crystal slab. For this reason, the photonic crystal is omitted entirely in the region adjacent to the tapered length of the feed.

Aside from matching, we must address the other, field-distribution requirement of the feed. To this end, we insert the tapered feed a short, finite distance into the lens body. This is because the approximate location of the feed's radiation center is situated inside the volume of the taper, rather than at its termination. Thus, the feed must be oriented such that this radiation center is as close as possible to the circumference of the lens body. In this way, the tapered feed mimics the behavior of a circumferential point source.

Taking the above empirical discussion of the feed structure into account, it is clear that there are three geometric parameters in the design of the feed; the total length of the taper, the width of the taper at its termination, and the insertion length into the lens body. A suitable design is found when these parameters are 2.325 mm, 100  $\mu\text{m}$ , and 325  $\mu\text{m}$ , respectively. These values are the result of a careful process of manual adjustment, which is preferable to automated algorithmic optimization due to the long simulation times that are associated with the electrically large antenna structure, as detailed in the [supplementary material](#). These chosen parameters are indicated in the diagram in Fig. 3. It is noted that this is not necessarily the best possible design for the feed. Rather, it is a design that is shown by simulations and experiments to exhibit acceptable behavior over the required bandwidth. Future designs may explore the use of other tapered profiles, such as exponential or spline curves, in order to determine whether this improves performance.

Finally, we observe that the taper is very thin and narrow and that silicon is a brittle material. Thus, if this were the only point of contact between the photonic crystal slab and the lens body, it would be vulnerable to breakage. So, in aid of mechanical stability, we extend the effective medium at the circumference of the Luneburg lens such that it meets with the photonic crystal, thereby uniting the two components within a single dielectric slab. As the effective modal index is quite low in this region, this addition is not expected to significantly impact the functionality of the antenna.

### III. CHARACTERIZATION

#### A. Fabrication

The antenna is fabricated together with the photonic crystal waveguide, in the same subtractive manufacture process. This consists of photolithography and plasma etching of a 4-in. single-crystal intrinsic silicon wafer of  $\sim 20$  k $\Omega$ -cm resistivity,<sup>3</sup> yielding vertical-walled through-holes of high quality. The similarity of hole diameters used for the structure, which range from 100 to 144  $\mu\text{m}$ , is beneficial to the quality of the etch, as the required parameters for the etch process typically vary with respect to hole size. Additionally, the use of intrinsic silicon of this sort engenders efficient devices, as it is a low-loss dielectric material.<sup>12</sup>

Two Luneburg-lens antennas are fabricated in this way. The first has just one port, and hence it does not exhibit the multi-beam functionality that is a salient feature of the Luneburg lens. This design is fabricated in order to verify that the Luneburg lens functions as intended, free from added complexities and potential confounding factors that may be introduced by the use of multiple ports. The second antenna has seven ports, which are spaced  $20^\circ$  apart, and hence it covers a  $120^\circ$  field of view. A photograph of each antenna is given in Fig. 4, and it can be seen that the lens body, waveguide track, and tapered feed are all well-defined. Additionally, the opposing end of each waveguide terminates in a tapered spike in order to facilitate coupling with a hollow metallic waveguide, for experimental characterization purposes. A linear taper is selected for this purpose, as opposed to an exponential curve, as it is more physically robust. For the seven-port design, care is taken to ensure that the physical separation between adjacent spikes is sufficient to prevent collision between the hollow metallic waveguide flange and a neighboring spike. This clearance can be increased by employing longer photonic crystal waveguide sections or by reducing the overall number of ports. That said, this concern is only relevant for the characterization of the antenna in isolation; in a practical system, active components would be integrated directly into the photonic crystal waveguide platform, thereby mitigating this issue of waveguide-flange clearance altogether.

As photonic crystal waveguides exhibit evanescent fields, they hold the potential to couple and exchange energy if they are situated in close proximity to each other. It is of interest to know whether this phenomenon impacts the performance of the seven-port Luneburg lens antenna. Previously, we have determined that the strength of near-field coupling between adjacent photonic crystal waveguides decreases rapidly with respect to the distance between them.<sup>25</sup> In the cited work, a directional coupler was realized with parallel photonic crystal waveguides separated by two rows of photonic crystal, but coupling strength falls by a factor of five when the number of separating rows is four and by a factor of twenty for six rows. For the seven-port Luneburg lens antenna that is covered in this work, adjacent

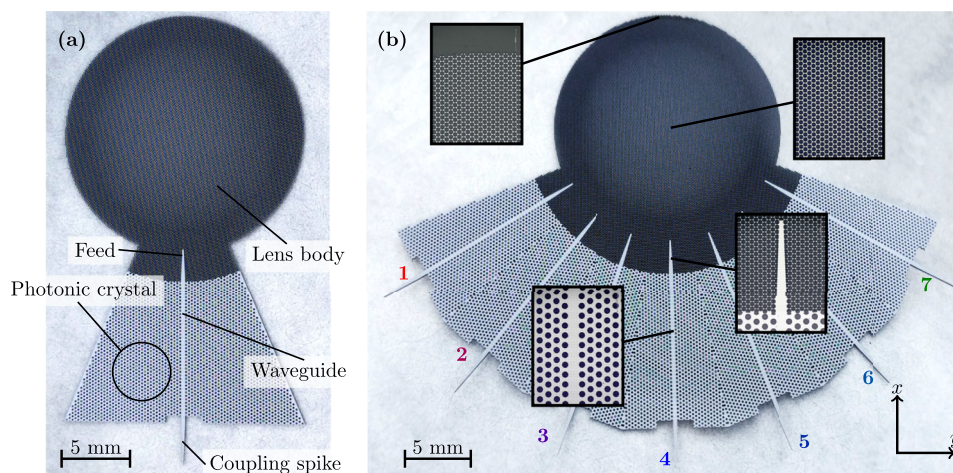


FIG. 4. Photographs of terahertz-range Luneburg-lens antennas. (a) One-port design, with labels indicating key components of the Luneburg-lens antenna, and (b) seven-port design, where ports are numbered counter-clockwise from the left, and inset micrographs show certain sections of the structure in more detail.



waveguides are separated by more than ten rows of photonic crystals at their closest point, and hence their interaction is expected to be essentially negligible; to implement the above directional coupler with ten rows of separation, one would need a coupled-line section that spans the entire diameter of the 4-in. wafer. That said, in order to be confident that waveguide interaction is tolerably low in a given application, one would need to analyze the particular needs of the system in question. Factors to consider include the relative quantity of power in adjacent lines, channel overlap, and the system's sensitivity to interference and phase noise.

## B. Simulation

In order to gain insight into the performance of the terahertz-range Luneburg-lens antenna, full-wave simulations that model the antenna in a transmitting configuration are conducted using CST Microwave Studio's time-domain solver. Detailed information about these full-wave simulations is provided in the [supplementary material](#). Field plots are extracted from the simulation of the single-port antenna and are presented in Fig. 5. These plots show that the waves spread out in the lens body after emission from the feed point. Thereafter, the lower-index regions near the edge accelerate these divergent wavefronts relative to the central portion. Finally, planarized wavefronts are seen to exit the Luneburg lens, at the side opposite to the feed. Thus, these field plots confirm that the Luneburg lens operates as intended.

On the other hand, Fig. 5 also reveals some non-ideal aspects of this antenna's behavior. First, it is apparent that the lens does not make use of its entire physical aperture for radiation, resulting in a reduction of the overall directivity. Additional to that, un-desired fields ejected from the sides of the feed structure appear to enter the lens body and interfere with the desired fields therein. This can be ascribed to the evanescent fields that exist in the photonic crystal medium that surrounds the waveguide, and it is likely that this effect generates sidelobes and is detrimental to the overall antenna gain. Another such feature is the fact that the outgoing wavefronts are not perfectly planarized, as they appear to have a slight, concave curvature. As a consequence of this, the emitted waves will pass through a waist before propagating to the far-field, and this effect also reduces the overall antenna gain. It is also noted that this curvature is more pronounced for the 360 GHz-case shown in Fig. 5(b). This is because 360 GHz is farther from the design frequency of the lens than 330 GHz, and hence it experiences minor deviation from the desired distribution of refractive index due to the dispersion of the slab mode.

The simulated reflection magnitude in the antenna ports is given in Fig. 6. It is noted that the reflection coefficient of ports 5–7 of the seven-port design has not been given, as the antenna symmetry renders this redundant. It can be seen that the reflection is below  $-10$  dB across the 320–390 GHz range in all cases, and hence this confirms that the antennas are adequately matched

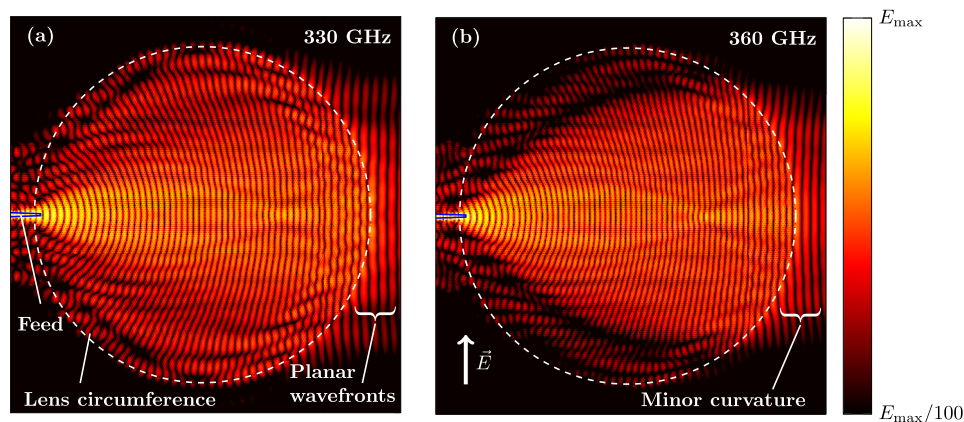


FIG. 5. Simulated results, showing electric field plots of the component that is in-plane and transverse to the orientation of the feed. In order to clearly show the evolution of the outgoing wavefront, these plots are logarithmic-scaled, instantaneous field-magnitude plots of the single-port design for (a) 330 and (b) 360 GHz, respectively. Each plot is normalized to its respective maximum.

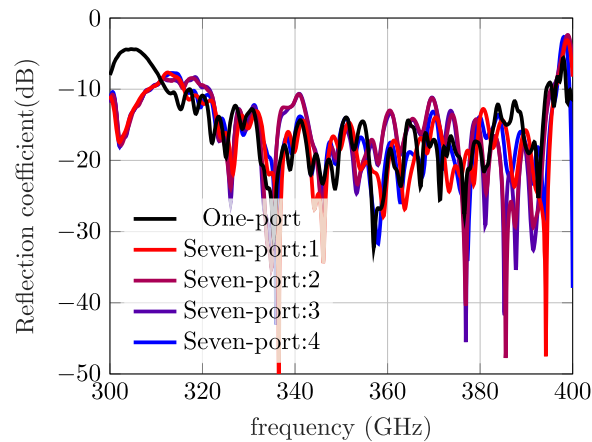


FIG. 6. Simulated reflection magnitude at the input ports of the antennas, where it is noted that ports 5–7 of the seven-port antenna are not shown due to redundancy.

over their operation bandwidth. It is noted that, for frequencies outside of this range, the photonic crystal exhibits a propagating mode.<sup>3</sup> A consequence is that some energy leaks from the waveguide into the slab at frequencies above 390 GHz, and also at frequencies below 315 GHz, to the detriment of matching. This effect limits the bandwidth of the Luneburg-lens antenna.

### C. Measured radiation characteristics

The Luneburg-lens antennas are characterized with the experimental setup that is given in Fig. 7. In this setup, the free-standing antennas are held with ordinary tweezers, and their characteristics are probed with electronic devices exclusively. First, a synthesizer generates a continuous wave, which

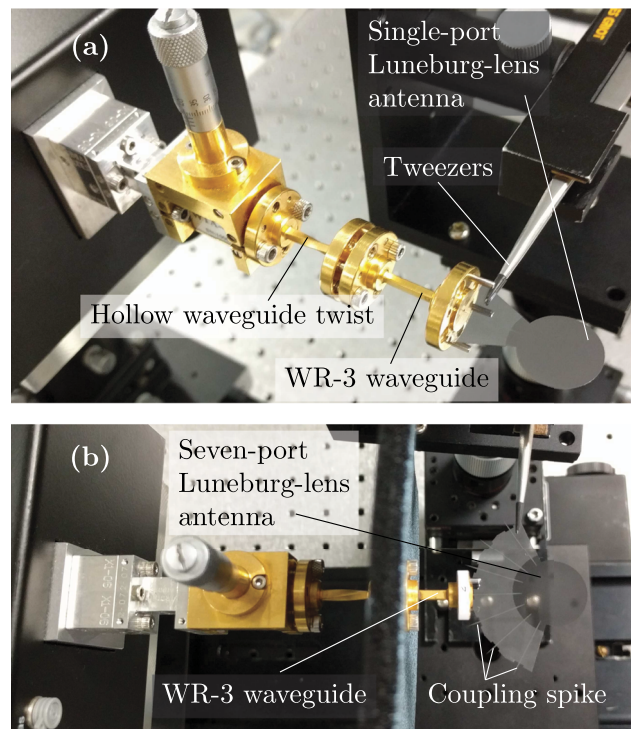


FIG. 7. Experimental setup. (a) The one-port Luneburg-lens antenna and (b) the seven-port Luneburg-lens antenna. Both are coupled to the terahertz radiation source via hollow rectangular waveguides. It is clear from these images that the antennas are free-standing, as they are both held with tweezers.

is tuned from 33.3 to 43.3 GHz. This signal is used to drive a  $\times 9$  multiplier, which outputs terahertz-range power from 300 to 390 GHz. This power is subsequently applied to the relevant port of the antenna under test, via a WR-3 rectangular waveguide, as indicated in Fig. 7(a). Thus, the Luneburg-lens antenna serves as a transmitter in the experiment. In order to couple the Luneburg-lens antenna to this rectangular waveguide, the dielectric spike at the end of the waveguide track, which is clearly visible in Fig. 4, is inserted directly into the hollow waveguide. The gradual taper of the spike provides broadband and efficient mode conversion between the two waveguides. The radiation that is emitted by the Luneburg-lens antenna subsequently propagates a free-space distance of  $\sim 30$  cm, whereupon it is received by a WR-3-coupled diagonal horn antenna. At the receiver side, a mixer with a built-in  $\times 36$  multiplier is used with a spectrum analyzer to amplify and down-convert the received terahertz signal to the microwave range.

In order to measure radiation patterns, the above process is carried out repeatedly and alternated with  $1^\circ$  steps on an automated, goniometric rotation stage. Waveguide twists are employed to select between the *E*- and *H*-planes. Thus, the radiated power is sampled as a function of angle, for both planes, and normalized by its maximum value in order to yield radiation patterns. The results of this procedure for the single-port antenna are given in Fig. 8 (Multimedia view). Radiation patterns

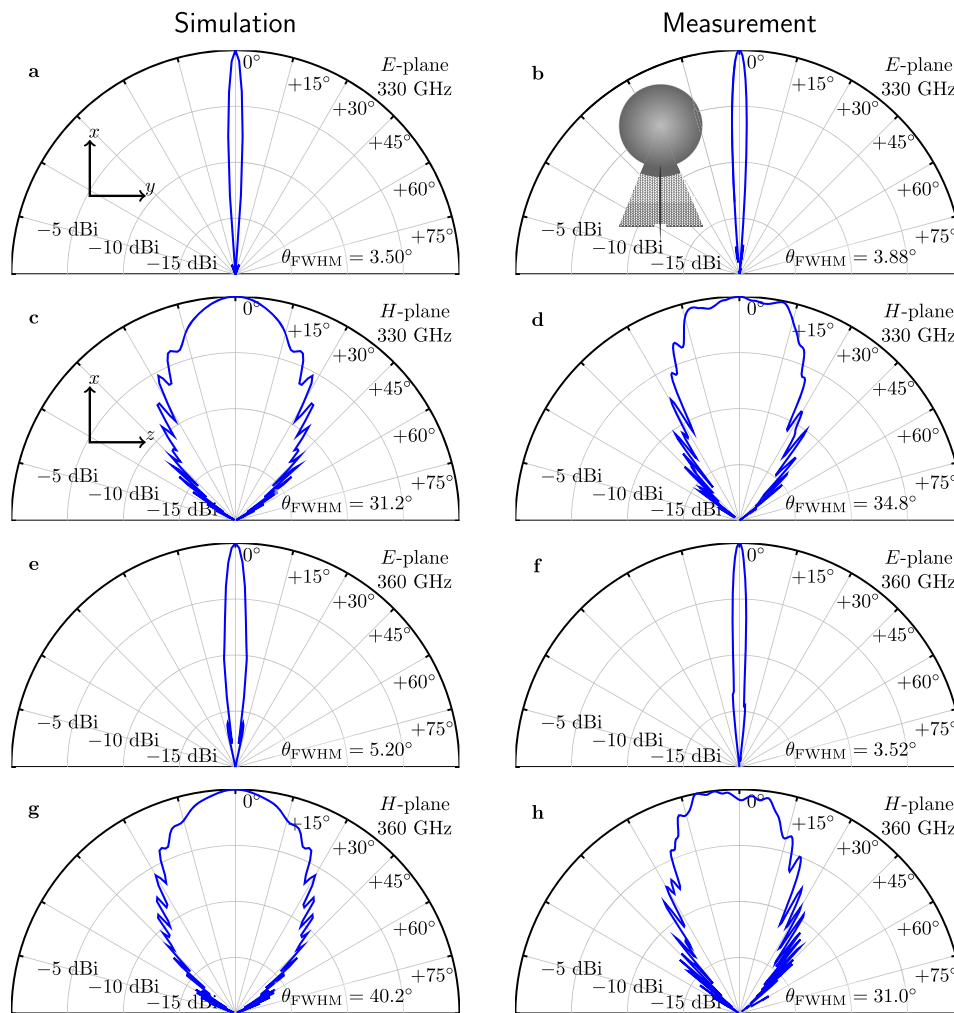


FIG. 8. Simulated and measured radiation patterns of the single-port Luneburg-lens antenna, showing [(a) and (b)] *E*-plane at 330 GHz, [(c) and (d)] *H*-plane at 330 GHz, [(e) and (f)] *E*-plane at 360 GHz, and [(g) and (h)] *H*-plane at 360 GHz. The divergence of each of the measured radiation patterns is quantified by the full-width half maximum angle ( $\theta_{FWHM}$ ). The diagram inset to (b) indicates the antenna's orientation. Broadband simulated radiation patterns, which show a stable beam pattern over the operation bandwidth, are included in the linked video file. Multimedia view: <https://doi.org/10.1063/1.5060631>

are given in both  $xy$  and  $xz$ -planes, which are designated as the  $E$ - and  $H$ -planes of this antenna, respectively. These results are presented alongside numerically simulated radiation patterns.

There are a number of key features of the single-port antenna's radiation patterns that warrant explanation. First, it is evident that the antenna's angular divergence in the  $E$ -plane is far narrower than that in the  $H$ -plane. Quantitatively, the measured full-width half maximum angle,  $\theta_{\text{FWHM}}$ , differs by a factor of  $\sim 9$ . This characteristic "fan-beam" shape can be understood as a direct consequence of the dimensions of the antenna aperture. In general, a larger antenna aperture is associated with a lower beam divergence.<sup>57</sup> This particular antenna spans 17 mm in the  $y$ -dimension, which is tangential to the  $E$ -plane, and 200  $\mu\text{m}$  in the  $z$ -dimension, and this bias towards the  $E$ -plane aperture is the origin of the aforementioned "fan-beam" shape. Another feature of these radiation patterns is finite ripple in the  $H$ -plane. This can be ascribed to the interference between the primary radiation surface (i.e., the output of the lens body) with weak, un-desired leakage from other components of the Luneburg-lens antenna, including the photonic crystal waveguide, and the transitions at both of its ends. It is noted that this pattern of ripples is not strictly consistent between the measured and simulated results, and this minor discrepancy can be ascribed to imperfect alignment. Furthermore, for an antenna of this size, the far-field begins at a 60–75 cm distance, and hence the receiver is not in the far-field of the Luneburg-lens antenna. Thus, if the radiation pattern were probed in the far-field, then the agreement between the simulation and measurement may be closer. Finally, we note the overall similarity between the results at 330 GHz and 360 GHz, which is a testament to the antenna's stable performance over its operation bandwidth.

The radiation patterns of the seven-port Luneburg-lens antenna are characterized, and the results are given in Fig. 9. It is noted that only ports 1–4 are probed directly for this purpose, and the  $E$ -field radiation patterns of ports 5–7 are contrived from the results of ports 1–3 due to the symmetry of the antenna. It is clear from the  $E$ -plane results that all ports project beams into different directions, which are evenly spaced at  $20^\circ$  intervals. This successfully validates the multi-beam functionality of the Luneburg-lens antenna. It is also noted that, aside from these differences in directionality, all radiation patterns of the seven-port antenna are consistent with those of the single-port antenna, which are given in Fig. 8 (Multimedia view). This is an indication that the addition of multiple ports does not markedly degrade the overall performance of the antenna.

The broadband performance of these antennas is of interest, and hence their peak antenna gain is measured as a function of frequency. For these measurements, the above experimental procedure is repeated with the receiving antenna fixed in the direction of the transmitter's main lobe. This is first

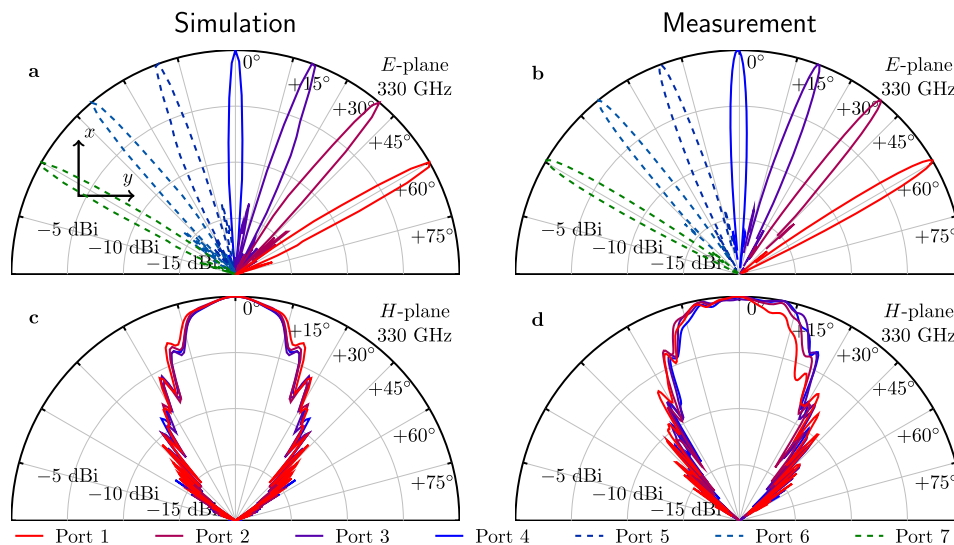


FIG. 9. Simulated and measured radiation patterns of all ports of the seven-port Luneburg-lens antenna at 330 GHz, [(a) and (b)]  $E$ -plane, and [(c) and (d)]  $H$ -plane, where the direction of each beam has been adjusted so as to align with the direction of maximum radiation.

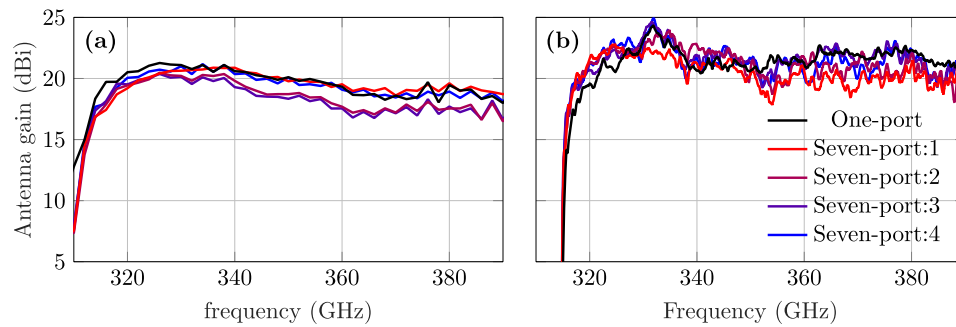


FIG. 10. Antenna gain in the direction of the main-lobe as a function of frequency, for the one- and seven-port designs, showing (a) simulated and (b) measured results.

performed for the Luneburg-lens antenna and then repeated with a standard-gain horn as transmitting antenna for calibration purposes. The antenna gain of the standard-gain horn is known, and hence this enables us to normalize the measured power by an established reference, in order to convert it into antenna gain. The results of this procedure are given in Fig. 10, and it can be seen that the measured antenna gain is greater than 20 dBi over the operation bandwidth for the one-port design and over 18 dBi for all measured ports of the seven-port antenna. The fact that the one-port design out-performs the seven-port design in this way is potentially due to minor scattering from adjacent ports in the latter design. That said, the performance of the two antennas is consistent overall, and hence we expect their beam-shapes and angular divergence to be very similar.

It is noted that there is a discrepancy between the measured and simulated results; the measured gain is consistently around 3 dBi higher than in simulation, and the results exhibit a common peak at 332 GHz that is not observed in simulation. This is likely due to the fact that the receiver is not in the far-field of the Luneburg-lens antenna. Furthermore, it can be seen from Figs. 5(a) and 5(b) that the outgoing wavefront exhibits a slight concave curvature, as has previously been noted. A consequence of this is that the beams must pass through a waist, in which the fields are concentrated, before they head out to the far-field. As our receiving antenna is situated prior to the far-field boundary, our measurement is impacted by this concentration effect, and hence the apparent measured field strength is increased. On the other hand, if the receiving antenna were truly in the far-field, then the beam would have passed through its waist long before reception, thereby mitigating this effect. This explanation can also account for the minor peak at 332 GHz that is only observed in the measurement. It is likely that, at this frequency, the beam waist is close to the aperture of the receiving antenna, and this leads to a greater proportion of radiated fields being received. On the other hand, the wavefront is more planar at lower frequencies, and hence the beam waist is at a greater distance. At higher frequencies, the beam waist is situated in-between the transmitter and receiver, and a consequence of this is that the fields are divergent by the time that they reach the receiver, leading to lower observed antenna gain.

For the seven-port design, it is desirable to know whether cross talk impacts performance. Unfortunately, it is not possible to simulate the interaction between different ports due to reasons that are detailed in the [supplementary material](#). Thus, we must rely exclusively upon experimental methods in order to characterize cross talk. To this end, two hollow rectangular waveguides are coupled to two separate ports of the antenna simultaneously. One such hollow waveguide is stimulated with terahertz power, and the power that is accepted by the other waveguide is measured. This measured power is representative of the cross talk between the relevant ports of the Luneburg-lens antenna. As in the previously detailed experiments, a microwave synthesizer and multiplier chain are employed to generate the terahertz-range power, and a mixer and spectrum analyzer are utilized for detection. In order to calibrate this measurement, the two hollow rectangular waveguides are then coupled directly together, and the measured power transmission in this configuration is employed to normalize the cross talk measurements. However, due to required clearances, we are unable to characterize the cross talk between close ports in this way. That said, we anticipate that cross talk is more severe for further-apart port pairs, as their radiation directions are closer to the pathological case of being in

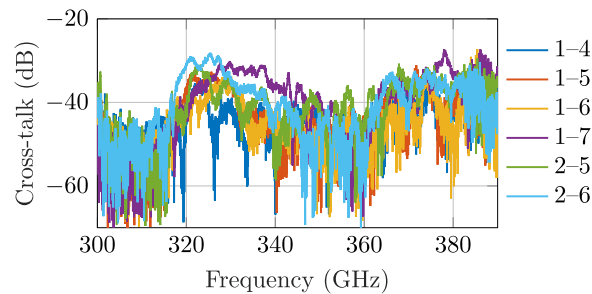


FIG. 11. Measured cross talk between pairs of ports in the seven-port Luneburg-lens antenna. Certain port pairs, such as 4–7, are excluded from this measurement as they are redundant due to symmetry. Other port pairs, such as 1–2, are also excluded as they cannot be simultaneously coupled to the probing waveguides due to physical clearances.

anti-parallel, i.e., pointing directly towards each other. The experimental results are shown in Fig. 11, and it can be seen that cross talk is below  $-28$  dB across the entire frequency range of interest, for all port-pairs that are thus characterized. This means that cross talk accounts for less than 0.16% of stimulated power.

#### IV. DEMONSTRATION OF TERAHERTZ COMMUNICATIONS

A prospective application of terahertz multi-beam antennas is high-volume communications. In order to validate the compatibility of the Luneburg-lens antenna with this application, we demonstrate the transfer of multi-Gb/s data using this antenna as transmitter. In contrast to the all-electronic system that is employed to measure radiation patterns and antenna gain, we make use of an optoelectronic system for this purpose so as to benefit from high-speed optical modulation.<sup>38</sup> For the transmitted signal, a two-color near-infrared optical laser signal, with a beat frequency of 335.5 GHz, is modulated using on-off keying (OOK). Subsequently, a nonlinear system consisting of an erbium-doped fiber amplifier and a uni-travelling carrier photodiode is employed to down-convert this modulated signal to the terahertz range.<sup>58</sup> This down-conversion generates power at the terahertz-range beat frequency, by extracting the envelope of the beating signal. As such, the amount of terahertz power that is generated is strongly dependent upon the amplitude of the incident laser excitation. Following down-conversion, the terahertz signal is transmitted through the Luneburg-lens antenna and radiated to free-space. Finally, this radiation is collected by a diagonal horn antenna, and a Schottky barrier diode is employed to extract the bit stream via envelope detection.

The transmission distance of this link is short—just 5 mm—and is restricted by the power that is available from the terahertz photonic source. It is noted that higher-power compact sources have previously been demonstrated in the literature,<sup>59,60</sup> and hence there is potential to increase this distance in the future. As 5 mm is not a far-field distance for either antenna, it is not possible to calculate the overall transmission of the link using methods such as the Friis transmission equation.<sup>61</sup> For this reason, we estimate the coupling efficiency numerically, via the normalized cross correlation of two-dimensional field aperture distributions that are extracted from numerical simulations of each antenna. The resulting coupling efficiency is  $\sim 20\%$ , which is a detriment to the received signal-to-noise ratio and reduces the achievable data rate of the link.

So as to evaluate the antenna's performance in this setup, the bit error rate of the link is measured under different conditions of transmitter power and data rate with OOK modulation. For this purpose, a pulse-pattern generator is employed as the data source for the optical modulator, and the demodulated signal is sent to a bit error-rate tester to verify reliable reception. First, a data rate of 6 Gb/s is maintained, and the amount of terahertz power that is applied to the input port of the Luneburg-lens antenna is varied. The results of this procedure are given in Fig. 12(a). It is found that the data are most reliably received when terahertz power is highest, which is to be expected, as higher input power engenders a greater signal-to-noise ratio at the receiver. The measured bit error rate in this case is less than  $10^{-11}$ , which is generally considered to be error-free transmission. Thereafter, the highest-power condition is maintained, and the transmitted data rate is varied. The results of this procedure are given

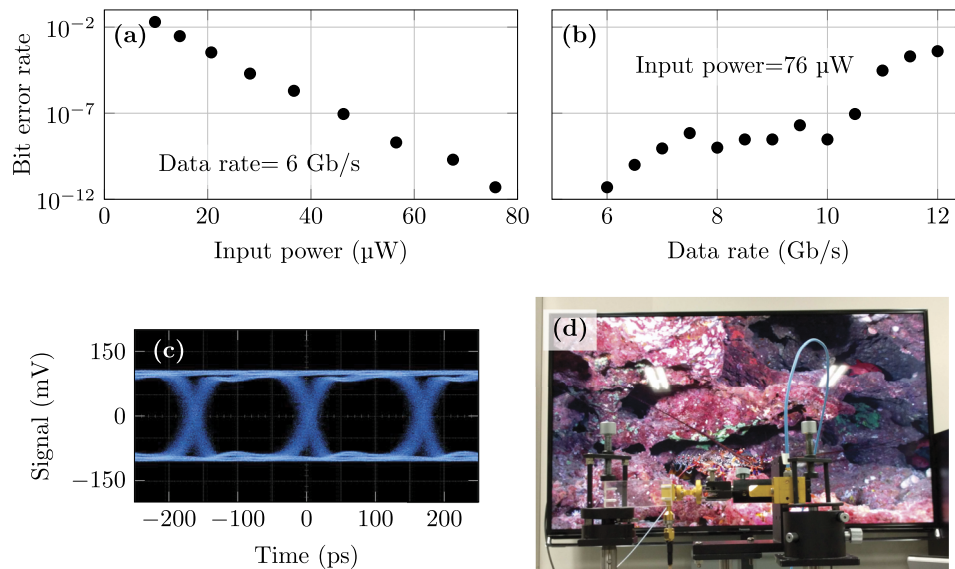


FIG. 12. Demonstration of short-range terahertz communications, showing (a) the relationship between the bit error rate and input terahertz power, (b) the relationship between the data rate and bit error rate, (c) eye diagram, corresponding to maximum power at 6 Gb/s, and (d) the transmission and reception of uncompressed 4K-resolution video at 6 Gb/s. It is noted that a three-port Luneburg-lens antenna is employed for this demonstration, due to practical, ease-of-experimentation factors. This antenna is essentially redundant with the seven-port device, and hence it is not covered in the main text. Multimedia view: (d) <https://doi.org/10.1063/1.5060631.2>

in Fig. 12(b), and it can be seen that an increase in the data rate produces a corresponding increase in the bit error rate. A contributing factor to this increase is that a higher data rate requires a larger signal-to-noise ratio. Thus, the fact that the available power is less than 100  $\mu\text{W}$  limits the achievable data rate of this short-range link.

An eye diagram is provided in Fig. 12(c), which corresponds to the case with highest terahertz power and modulating data rate of 6 Gb/s. This condition produces to the lowest bit error rate, which is evidenced by the fact that the “eye” is clearly open. Thus, we show that reliable, multi-Gb/s communications links are possible using the terahertz-range Luneburg-lens antenna. Furthermore, we assert that the achievable data rate is currently limited by low transmit power, as the antenna bandwidth indicated by Figs. 6 and 10 is sufficient to support 50 Gb/s with OOK modulation. Thus, utilizing a more powerful source with the Luneburg-lens antenna would likely yield a greater data rate.

In addition to the characterization of the bit error rate, we also demonstrate the reliable transmission and reception of uncompressed 4K video data, with a data rate of 6 Gb/s. The signal source is provided by a 4K video player, and the demodulated bit stream is subsequently routed to a television of the appropriate resolution and displayed in real-time. See Fig. 12 (Multimedia view) for a video of this experiment. A still frame from this video is included as Fig. 12(d).

## V. CONCLUSION

In this article, we have presented the all-silicon integration of a terahertz multi-beam planar Luneburg-lens antenna with photonic crystal waveguides. The antennas are designed to operate over a bandwidth that spans from 320 to 390 GHz. Two designs have been devised: a single-port design, which is intended to validate the beamforming functionality, and a seven-port design, which serves to demonstrate the desired multi-beam capabilities of the device.

Simulations show that the antennas are adequately matched over their operation bandwidth. Experimental results indicate antenna gain in excess of 18 dBi for all tested ports of both antennas, although it is noted that simulated results indicated marginally lower gain. Cross talk was

experimentally determined to be lower than  $-28$  dB. Finally, a demonstration of multi-Gb/s terahertz communications that made use of the Luneburg-lens antenna confirmed its potential for applications in high-speed communications links.

## VI. OUTLOOK

Where prospective applications are concerned, the multi-beam functionality of the terahertz Luneburg-lens antenna makes it possible for a single terahertz system to maintain a number of independent links concurrently. Thus, antennas of this sort may provide line-of-sight interconnect in a network of transceiver nodes, as illustrated in Fig. 13(a). This removes the necessity of a physical connection between adjacent nodes, and in doing so increases the node density. Thereafter, each node could be employed as a picocell in a terrestrial wireless network, where users access that network via established standards such as Long-Term Evolution (LTE) and WiFi, in order to provide high-speed internet access in areas of high population density. Aside from communications, the Luneburg-lens antenna may also find uses in short-range terahertz radar, as the antenna's broad bandwidth has the capacity to support fine-ranging resolution.<sup>62</sup> Thus, it is anticipated that multi-beam antennas such as this will lead to short-range terahertz radar devices that monitor several directions simultaneously, as illustrated in Fig. 13(b).

Two possible extensions to this antenna are improvements to antenna gain, and increasing the number of angles inside the  $120^\circ$  arc that are accessible to the device. For the first aim, it may be possible to refine the feed structure such that the overall aperture efficiency of the Luneburg lens is increased. For the second aim, it is noted that the antenna gain of the seven-port Luneburg-lens antenna is slightly lower than that of the single-port antenna, due to minor scattering from adjacent feeds. Increasing the density of feeds around the circumference is likely to exacerbate this effect, and hence care must be taken to avoid excessive degradation of antenna gain when improving the angular resolution. On the other hand, if the diameter of the lens were to be made larger, then this would simultaneously improve antenna gain and increase the achievable number of ports with a given spacing. The antennas that are reported in this article are fabricated from a 4-in. wafer, and hence there is sufficient available area to fabricate a lens with 5–6 times larger aperture. That said, the main constraining factor of the gain of this device is its planar structure; it can only achieve broad aperture in one dimension. Thus, in order to develop truly high-gain antennas, we must expand to radiating apertures for which size can be increased in both transverse dimensions. Finally, we note that, although the antenna that is presented in this work is a stand-alone device that is coupled to hollow metallic waveguides, our ultimate aim is to implement

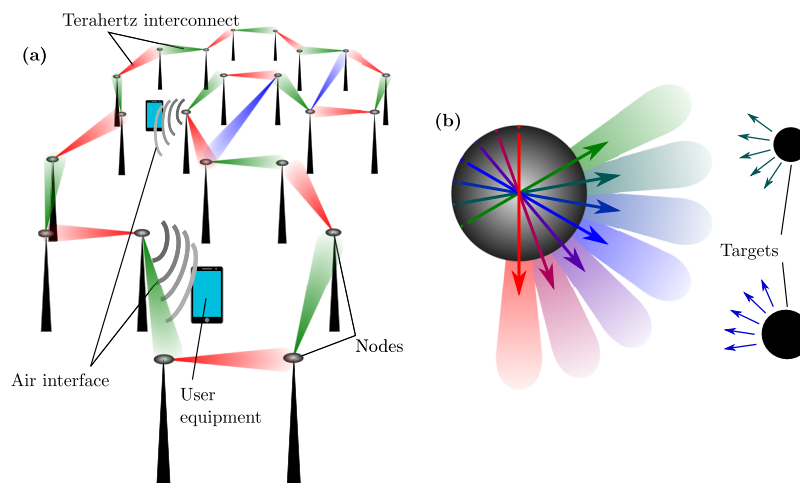


FIG. 13. Prospective applications of multi-beam terahertz antennas, showing (a) a communications application, where individual multi-beam antennas support the interconnect between multiple picocell nodes simultaneously for high-density frequency reuse in the air interface. (b) Envisaged short-range terahertz radar concept using multi-beam antenna.



entire terahertz systems that realize these applications in the same photonic crystal waveguide platform.

## SUPPLEMENTARY MATERIAL

See [supplementary material](#) for detailed information about the numerical simulations that are employed in this work and a brief exploration of the dependence of the Luneburg lens antenna's beamwidth upon frequency.

## ACKNOWLEDGMENTS

We wish to acknowledge support from the following grants: Core Research for Evolutional Science and Technology (CREST) program, Japan Science and Technology Agency (JST) (Grant No. JPMJCR1534); Grant-in-Aid for Scientific Research, the Ministry of Education, Culture, Sports, Science and Technology of Japan (Grant No. 17H01064); and Australian Research Council Discovery Projects (Grant Nos. ARC DP170101922 and DP180103561). The Quadro P6000 GPU used for this research was donated by the NVIDIA Corporation to the Terahertz Engineering Laboratory, The University of Adelaide. The authors would like to thank Mr. Xionbin Yu, Mr. Yuki Kimura, Mr. Yousuke Nishida, and Mr. Thomas Bücher for their assistance.

## APPENDIX: DETAILS OF LUNEBURG-LENS DESIGN

Analytical solutions exist for the required distribution of refractive index in a Luneburg-lens antenna with arbitrary edge-index  $n_0$ .<sup>46,50</sup> These take the form of a set of parametric equations that are dependent upon the parameter  $\alpha$ , which is the product of refractive index and normalized lens radius

$$\alpha = n \frac{r}{r_{\max}}. \quad (\text{A1})$$

From this equation, we can see that  $\alpha = n_{\max} \times (0/r_{\max}) = 0$  at the lens center and that  $\alpha = n_0 \times (r_{\max}/r_{\max}) = n_0$  at its edge. Thus,  $\alpha$  is treated as an independent variable that ranges from 0 to  $n_0$ , and both refractive index,  $n$ , and normalized radius,  $r/r_{\max}$ , are treated as functions thereof.

In order for a Luneburg lens to exhibit its characteristic focusing behavior, the refractive index must vary with  $\alpha$  according to the following relation:

$$n(\alpha) = \begin{cases} n_0 \left( \sqrt{1 + \sqrt{1 - \alpha^2}} \right) \exp(-\Omega(\alpha)), & \text{if } \alpha \leq 1, \\ n_0 & \text{if } \alpha > 1, \end{cases} \quad (\text{A2})$$

where

$$\Omega(\alpha) = \frac{2}{\pi} \int_{\frac{1}{n_0}}^1 \frac{1}{r'} \arctan \left( \sqrt{\frac{1 - \alpha^2}{(n_0 r')^2 - 1}} \right) dr'. \quad (\text{A3})$$

Thus, the procedure to determine the required index distribution for a given edge-index  $n_0$  begins with numerically solving the integral in Eq. (A3) to yield  $\Omega(\alpha)$ , which is subsequently deployed in Eq. (A2) in order to obtain refractive index as a function of the parameter  $\alpha$ . Thereafter, the corresponding normalized radius,  $r/r_{\max}$ , is extracted straightforwardly for each value of  $\alpha$ , by re-arranging Eq. (A1),

$$\frac{r}{r_{\max}} = \frac{\alpha}{n}. \quad (\text{A4})$$

As we now have both refractive index and normalized radius as functions of  $\alpha$ , this provides a mapping between the refractive index and position. The resultant distribution of refractive index can be scaled to any desired value of maximum radius. Finally, it is noted that the conditional statement in Eq. (A2) gives rise to the slope discontinuity that is seen in Fig. 2.

In order to model the behavior of the silicon slab, which is perforated with a dense array of subwavelength air holes, we make use of a two-dimensional version of the Maxwell Garnett effective medium approximation.<sup>38,52</sup> There are two media that are mixed in this way: air, with relative

permittivity of unity, and high-resistivity silicon, which has relative permittivity  $\epsilon_{\text{Si}} = 11.68$ .<sup>12</sup> In this case, the effective medium approximation yields the following effective relative permittivity:

$$\epsilon_{\text{eff}} = n_{\text{eff}}^2 = \epsilon_{\text{Si}} \frac{(1 + \epsilon_{\text{Si}}) + (1 - \epsilon_{\text{Si}})\zeta}{(1 + \epsilon_{\text{Si}}) - (1 - \epsilon_{\text{Si}})\zeta}, \quad (\text{A5})$$

where  $\zeta$  is the volumetric fill factor of the air in the silicon. For a triangular lattice of cylindrical through-holes,  $\zeta$  can be calculated geometrically. If the cylinder diameter is  $D$ , and the lattice constant is  $a$ , then the fill factor is given by the area ratio of a semicircle with diameter  $D$  and an equilateral triangle of sidelength  $a$

$$\zeta = \frac{\pi D^2}{2\sqrt{3} a^2}. \quad (\text{A6})$$

It is noted that Eq. (A5) is valid only when the electric field vector is orthogonal to the orientation of the cylinders. Furthermore, this model is dependent on the validity of the effective medium theory approximation, which requires that the periodicity of the hole spacing remains subwavelength. As such, this model will ultimately break down as frequency is increased beyond the point where the perforations can no longer be considered subwavelength. Thereafter, it may exhibit behavior similar to the photonic crystal medium.

The phase constant,  $\beta_m$ , of a  $\text{TE}_m$  mode in a dielectric slab of thickness  $t$  and bulk index  $n_{\text{eff}}$  is given in transcendental form as<sup>56</sup>

$$\tan^2 \left\{ \frac{t}{2} \sqrt{(n_{\text{eff}} k_0)^2 - \beta_m^2} - \frac{m\pi}{2} \right\} = \frac{\beta_m^2 - k_0^2}{(n_{\text{eff}} k_0)^2 - \beta_m^2}, \quad (\text{A7})$$

where  $k_0$  is the free-space wavenumber. After extracting the phase constant from this equation, the corresponding effective modal index,  $n_{\text{wg},m}$ , is given by

$$n_{\text{wg},m} = \frac{\beta_m}{k_0}. \quad (\text{A8})$$

The mode in which the wave propagates in the planar Luneburg lens is a  $\text{TE}_0$  mode. Thus, the effective bulk index is calculated from the geometric layout of the hole lattice effective medium using Eq. (A5). This bulk index is translated to a modal index using Eqs. (A7) and (A8), and this modal index is employed in the design of the Luneburg lens, according to Eqs. (A1)–(A4).

- <sup>1</sup> C. Yee, N. Jukam, and M. Sherwin, *Appl. Phys. Lett.* **91**, 194104 (2007).
- <sup>2</sup> R. Kakimi, M. Fujita, M. Nagai, M. Ashida, and T. Nagatsuma, *Nat. Photonics* **8**, 657 (2014).
- <sup>3</sup> K. Tsuruda, M. Fujita, and T. Nagatsuma, *Opt. Express* **23**, 31977 (2015).
- <sup>4</sup> H. Amarloo and S. Safavi-Naeini, *IEEE Trans. Terahertz Sci. Technol.* **7**, 433 (2017).
- <sup>5</sup> W. Withayachumnankul, M. Fujita, and T. Nagatsuma, *Adv. Opt. Mater.* **6**, 1800401 (2018).
- <sup>6</sup> S. J. McNab, N. Moll, and Y. A. Vlasov, *Opt. Express* **11**, 2927 (2003).
- <sup>7</sup> Y. Akahane, T. Asano, B. S. Song, and S. Noda, *Nature* **425**, 944 (2003).
- <sup>8</sup> M. Notomi, A. Shinya, S. Mitsugi, E. Kuramochi, and H. Ryu, *Opt. Express* **12**, 1551 (2004).
- <sup>9</sup> Y. Jiang, W. Jiang, L. Gu, X. Chen, and R. T. Chen, *Appl. Phys. Lett.* **87**, 221105 (2005).
- <sup>10</sup> L. O'Faolain, X. Yuan, D. McIntyre, S. Thoms, H. Chong, R. M. De La Rue, and T. F. Krauss, *Electron. Lett.* **42**, 1454 (2006).
- <sup>11</sup> T. Baba, *Nat. Photonics* **2**, 465 (2008).
- <sup>12</sup> J. Dai, J. Zhang, W. Zhang, and D. Grischkowsky, *J. Opt. Soc. Am. B* **21**, 1379 (2004).
- <sup>13</sup> P. Drude, *Ann. Phys.* **306**, 566 (1900).
- <sup>14</sup> S. Atakaramians, S. Afshar, T. M. Monro, and D. Abbott, *Adv. Opt. Photonics* **5**, 169 (2013).
- <sup>15</sup> C. Yeh, F. Shimabukuro, and P. H. Siegel, *Appl. Opt.* **44**, 5937 (2005).
- <sup>16</sup> K. R. Jha and G. Singh, *J. Comput. Electron.* **10**, 186 (2011).
- <sup>17</sup> S. Makhlof, B. Khani, J. Lackmann, S. Dülme, and A. Stöhr, in *1st International Workshop on Mobile Terahertz Systems (IMWTS)* (IEEE, 2018).
- <sup>18</sup> A. von Bieren, E. De Rijk, J.-P. Ansermet, and A. Macor, in *39th International Conference on Infrared, Millimeter, and Terahertz waves (IRMMW-THz)* (IEEE, 2014).
- <sup>19</sup> M. Sugeta, M. Fujita, and T. Nagatsuma, in *Proceedings of 79th Japan Society of Applied Physics (JSAP) Autumn Meeting, 2018*, 20p-212A-15.
- <sup>20</sup> M. Navarro-Cía, J. E. Melzer, J. A. Harrington, and O. Mitrofanov, *J. Infrared, Millimeter, Terahertz Waves* **36**, 542 (2015).
- <sup>21</sup> W. Otter, N. Ridler, H. Yasukochi, K. Soeda, K. Konishi, J. Yumoto, M. Kuwata-Gonokami, and S. Lucyszyn, *Electron. Lett.* **53**, 471 (2017).
- <sup>22</sup> M. Goto, A. Quema, H. Takahashi, S. Ono, and N. Sarukura, *Jpn. J. Appl. Phys.* **43**, L317 (2004).
- <sup>23</sup> J.-Y. Lu, C.-P. Yu, H.-C. Chang, H.-W. Chen, Y.-T. Li, C.-L. Pan, and C.-K. Sun, *Appl. Phys. Lett.* **92**, 064105 (2008).

- <sup>24</sup> X. Yu, R. Yamada, J.-Y. Kim, M. Fujita, and T. Nagatsuma, in 40th Progress In Electromagnetics Research Symposium (PIERS), 2018, SC3–2A16–1.
- <sup>25</sup> M. Yata, M. Fujita, and T. Nagatsuma, *Opt. Express* **24**, 7835 (2016).
- <sup>26</sup> C. M. Yee and M. S. Sherwin, *Appl. Phys. Lett.* **94**, 154104 (2009).
- <sup>27</sup> W. J. Otter, S. M. Hanham, N. M. Ridler, G. Marino, N. Klein, and S. Lucyszyn, *Sens. Actuators, A* **217**, 151 (2014).
- <sup>28</sup> S. Hanham, C. Watts, W. Otter, S. Lucyszyn, and N. Klein, *Appl. Phys. Lett.* **107**, 032903 (2015).
- <sup>29</sup> K. Okamoto, K. Tsuruda, S. Diebold, S. Hisatake, M. Fujita, and T. Nagatsuma, *J. Infrared, Millimeter, Terahertz Waves* **38**, 1085 (2017).
- <sup>30</sup> K. Tsuruda, K. Okamoto, S. Diebold, S. Hisatake, M. Fujita, and T. Nagatsuma, in 37th Progress in Electromagnetics Research Symposium (PIERS) (IEEE, 2016), pp. 3922–3926.
- <sup>31</sup> S. Diebold, K. Nishio, Y. Nishida, J.-Y. Kim, K. Tsuruda, T. Mukai, M. Fujita, and T. Nagatsuma, *Electron. Lett.* **52**, 1999 (2016).
- <sup>32</sup> S. Diebold, K. Tsuruda, J.-Y. Kim, T. Mukai, M. Fujita, and T. Nagatsuma, *Proc. SPIE* **9856**, 98560U (2016).
- <sup>33</sup> S. Diebold, S. Nakai, K. Nishio, J. Kim, K. Tsuruda, T. Mukai, M. Fujita, and T. Nagatsuma, *IEEE Trans. Terahertz Sci. Technol.* **6**, 716 (2016).
- <sup>34</sup> D. Taillaert, W. Bogaerts, P. Bienstman, T. F. Krauss, P. Van Daele, I. Moerman, S. Verstyuyt, K. De Mesel, and R. Baets, *IEEE J. Quantum Electron.* **38**, 949 (2002).
- <sup>35</sup> L. Liu, M. Pu, K. Yvind, and J. M. Hvam, *Appl. Phys. Lett.* **96**, 051126 (2010).
- <sup>36</sup> A. Michaels and E. Yablonovitch, *Opt. Express* **26**, 4766 (2018).
- <sup>37</sup> W. Withayachumnankul, R. Yamada, C. Fumeaux, M. Fujita, and T. Nagatsuma, *Opt. Express* **25**, 14706 (2017).
- <sup>38</sup> W. Withayachumnankul, R. Yamada, C. Fumeaux, M. Fujita, and T. Nagatsuma, *APL Photonics* **3**, 051707 (2018).
- <sup>39</sup> D. Headland, Y. Monnai, D. Abbott, C. Fumeaux, and W. Withayachumnankul, *APL Photonics* **3**, 051101 (2018).
- <sup>40</sup> W. Rotman and R. Turner, *IEEE Trans. Antennas Propag.* **11**, 623 (1963).
- <sup>41</sup> L. T. Hall, H. J. Hansen, and D. Abbott, *Proc. SPIE* **4935**, 215–222 (2002).
- <sup>42</sup> R. K. Luneburg and M. Herzberger, *Mathematical Theory of Optics* (University of California Press, 1964).
- <sup>43</sup> C. Pfeiffer and A. Grbic, *IEEE Trans. Antennas Propag.* **58**, 3055 (2010).
- <sup>44</sup> M. Liang, W.-R. Ng, K. Chang, K. Gbele, M. E. Gehm, and H. Xin, *IEEE Trans. Antennas Propag.* **62**, 1799 (2014).
- <sup>45</sup> S.-G. Park, K. Lee, D. Han, J. Ahn, and K.-H. Jeong, *Appl. Phys. Lett.* **105**, 091101 (2014).
- <sup>46</sup> J. Hunt, N. Kundtz, N. Landy, V. Nguyen, T. Perram, A. Starr, and D. R. Smith, *Sensors* **11**, 7982 (2011).
- <sup>47</sup> A. Di Falco, S. C. Kehr, and U. Leonhardt, *Opt. Express* **19**, 5156 (2011).
- <sup>48</sup> L. H. Gabrielli and M. Lipson, *Opt. Express* **19**, 20122 (2011).
- <sup>49</sup> J. Hunt, T. Tyler, S. Dhar, Y.-J. Tsai, P. Bowen, S. Larouche, N. M. Jokerst, and D. R. Smith, *Opt. Express* **20**, 1706 (2012).
- <sup>50</sup> S. P. Morgan, *J. Appl. Phys.* **29**, 1358 (1958).
- <sup>51</sup> H. Looyenga, *Physica* **31**, 401 (1965).
- <sup>52</sup> A. V. Subashiev and S. Luryi, *J. Lightwave Technol.* **24**, 1513 (2006).
- <sup>53</sup> B. Ung, A. Dupuis, K. Stoeffler, C. Dubois, and M. Skorobogatiy, *J. Opt. Soc. Am. B* **28**, 917 (2011).
- <sup>54</sup> E. M. Cheng, M. F. B. A. Malek, M. Ahmed, K. Y. You, K. Y. Lee, and H. Nornikman, *Prog. Electromagn. Res.* **129**, 559 (2012).
- <sup>55</sup> D. Headland, P. Thurgood, D. Stavrevski, W. Withayachumnankul, D. Abbott, M. Bhaskaran, and S. Sriram, *Opt. Mater. Express* **5**, 1373 (2015).
- <sup>56</sup> B. E. Saleh and M. C. Teich, *Fundamentals of Photonics*, 2nd ed. (John Wiley and Sons, Inc., 2007).
- <sup>57</sup> C. A. Balanis, *Antenna Theory: Analysis and Design*, 4th ed. (John Wiley & Sons, 2016).
- <sup>58</sup> T. Nagatsuma, G. Ducournau, and C. C. Renaud, *Nat. Photonics* **10**, 371 (2016).
- <sup>59</sup> U. R. Pfeiffer, Y. Zhao, J. Grzyb, R. Al Hadi, N. Sarmah, W. Förster, H. Rucker, and B. Heinemann, *IEEE J. Solid-State Circuits* **49**, 2938 (2014).
- <sup>60</sup> R. Han, C. Jiang, A. Mostajeran, M. Emadi, H. Aghasi, H. Sherry, A. Cathelin, and E. Afshari, *IEEE J. Solid-State Circuits* **50**, 2935 (2015).
- <sup>61</sup> H. T. Friis, *Proc. IRE* **34**, 254 (1946).
- <sup>62</sup> M. I. Skolnik, *Radar Handbook*, 2nd ed. (McGraw-Hill Incorporated, 1990).